Experimental investigation of aerodynamics and structure of a swirl-stabilized kerosene spray flame with laser diagnostics

P. Malbois, Erwan Salaün, Alexis Vandel, G. Godard, G. Cabot, B. Renou, A. Boukhalfa, Frederic Grisch

Experimental Investigation of Aerodynamics and Structure of a Swirl-Stabilized Kerosene Spray Flame with Laser Diagnostics.

P. Malbois[1, 2*], E. Salaün[1, 3*], A. Vandel[1], G. Godard[1], G. Cabot[1], B. Renou[1], A. M. Boukhalfa[1], F. Grisch[1]

[1]: Normandie Univ., INSA Rouen, UNIROUEN, CNRS, CORIA, Rouen 76000, France
[2]: SAFRAN Tech, Paris-Saclay, France
[3]: SAFRAN Aircraft Engines, Moissy-Cramayel, France

Corresponding author: Frédéric Grisch

Mailing address: UMR 6614 CORIA
INSA de Rouen Normandie
Site Universitaire du Madrillet BP 12
76801 Saint-Etienne du Rouvray Cedex
France

Tel: +33 2 32 95 97 84
Email: frederic.grisch@coria.fr

Keywords: High-speed PIV, High-speed OH-PLIF, Turbulent swirled flame, atmospheric pressure, spray combustion, Aeronautical fuel injector, Kerosene.

Paper submitted to: Combustion and Flame

Abstract

A gas turbine model combustor was equipped with an industrial Lean Premixed fuel injection system operating with liquid commercial kerosene (Jet-A1) at atmospheric pressure. Large optical accesses enable joint Particle Image Velocimetry (PIV) and OH planar laser-induced fluorescence (PLIF) measurements at repetition rates up to 5 kHz and 10 kHz respectively. Using these diagnostics, flame topologies and non-stationary events were investigated in operating conditions representative of the ones encountered in real aeronautic propulsion systems. The flame shape was analyzed in terms of interactions between the different flame zones responsible for flame stabilization in confined swirled flames. Data processing of the strain rate and vorticity fields highlighted the existence of two shear layers that interfere differently with the inlet air/fuel mixing jet. An inner shear layer (ISL) between the Inner Recirculation Zone (IRZ) and the fresh inlet flow is located at the upper base of the fuel spray. An Outer Shear Layer (OSL) is also identified between the Outer Recirculation Zone (ORZ) and the fresh incoming flow. Spanwise-oriented vortices are produced from this latter, with a growth rate function of the free stream speed ratio (fresh incoming reactants and the flow circulating inside ORZ). The detailed analysis of the shear layers gives new insight on the flame structures obtained from OH-PLIF data. Finally, high-speed simultaneous measurements of flow velocity and OH distributions highlighted unusual flame pinching mechanisms leading to the release of subsequent unburned pockets propagating in the burned gases.

1 Introduction

Aero-engine emissions are becoming a global environmental issue as air traffic continues to rise. Environmental concerns and legislative regulations laid down by governing organizations are therefore driving aircraft combustor manufacturers to meet more stringent emission standards on NOx, CO and soot while maintaining or improving the efficiency and reliability of future aero-engine combustors. In the case of small operating pressure range aero-engines such as helicopter combustors, the concept of lean premixed (LP) combustion has been introduced as one of the best solutions to significantly reduce NOx emissions [1–4]. The LP concept is based on the action of two air flows, one devoted to the fuel atomisation and the second to mixing and fuel evaporation. Their combination acts as a promoter for the stabilisation of the flame in the combustion chamber. Too sharp a reduction in the emission of NOx can, unfortunately, lead automatically to a decline in flame stability as well as a drastic increase in CO and hydrocarbon (HC) emissions [5]. Generally, enhancement of the flame stabilization is provided by means of swirl flows. Swirling flames are commonly characterised by unsteady flow structures, including irregular highly turbulent motion and dynamics of coherent flow structures which interact with the flame downstream from the fuel injection system. Furthermore, the large expansion of the flow induced by the heat release rate can produce recirculation zones that promote the transportation of hot reaction products back to the flame base, thereby enhancing the local ignition of fuel and thus the flame stability. Between the inflow and recirculation zones, unsteady shear layers allow the mixing between fresh and hot gases. Finally, typical dynamics related to vortex breakdown, such as helical structures or Precessing Vortex Core (PVC) can be a source of flow and heat release rate unsteadiness which may trigger instabilities such as thermo-acoustic oscillations [6,7]. Of course, all of these physical processes may compete or interact together [8], which complicates their modelling. Further detailed experimental studies are then required to conduct a better comprehensive analysis of these interaction mechanisms in order to improve the performances of future aero-engine combustors.

In recent years, strong efforts have been made experimentally to improve the knowledge of the related phenomena and to explore ideas for circumventing flame stability issues in LP combustors. Effects of swirl on the flame structure were initially studied with laser diagnostics in GT model combustors powered by gaseous fuel

[9,10]. The role of PVC on the reaction zone under unstable conditions was also investigated using high-speed laser diagnostics [11]. Local interactions between the aerodynamic flowfield and the reaction zone in CH_4/air flames [7,11–13], thermo-acoustic oscillations/flow field interactions [9] and fuel-to-air mixing [14] were also addressed. More recently, high-speed PIV and OH-PLIF laser diagnostics were applied in a pressurized natural gas fuelled burner to study the flame/flow interactions in pressures up to 5 bar [15,16]. Unfortunately, all of these studies were only performed with gaseous fuels that are not realistic of operating conditions relevant to real aero-engine combustors. To better understand the physical processes that take place in relevant gas turbines, efforts were initiated by first investigating the effects of spray fuel injection on the flame characteristics. As an example, an experimental study on confined swirl flames fuelled by methane or kerosene fuels showed similarities in the aerodynamic flow properties in both flames but significant differences in the flame structures [17]. One explanation formulated by the authors was related to the combustion of liquid fuel droplets that modifies the diffusion of fuel vapour and oxidizer species and thus the reaction rates. The chemical properties of liquid fuels and their associated fuel atomization are also scalar parameters that change the characteristics of swirl combustion systems [18]. Indeed, the authors observed different droplet size distributions and flame structures when comparing biofuel (RME)/air and Jet-A1/air swirl spray flames. The lower viscosity and higher volatility of Jet-A1 then promote the fuel atomization leading to faster evaporation and better mixing while the velocity distributions in both flames are similar. The dynamics of swirled flames was also investigated using high-speed PIV and/or OH-PLIF laser diagnostics. For instance, various types of swirl-stabilized flames close to blow-off limits were studied by high-speed OH-PLIF [19]. The results of this study showed that spray swirl-stabilized flames are more sensitive to lift-off and local extinction than gaseous premixed swirl-stabilized flames. The timescale of the blow-off event was also shorter in spray flames than in premixed and non-premixed gaseous CH_4/air swirl-stabilized flames. Interaction between the fuel droplets and the aerodynamic conditions is also a mechanism that significantly affects the overall characteristics of swirl-stabilized spray flames [20]. The effect of pressure on swirled-stabilized spray flames is another physical parameter which has an influence on the flame characteristics. For instance, large interactions between the mean flame location and the aerodynamic flow field were underlined in a GT model combustor equipped with an LP injection system fuelled with kerosene at 4.5 bar [21]. Flame structure and

droplet distribution were also analysed at 3 bar by visualising the fuel and the OH distribution with high-speed PLIF in a gas turbine fuelled with various fuels such as Jet-A1 and biofuel [21]. Another work focused on the quantitative effect on the unsteadiness produced in LPP injection systems operated at various pressures (1 to 4.5 bar) with Jet-A1 fuel was investigated using PIV and PLIF diagnostics [8]. More recently the interaction between fuel vapour and liquid, aerodynamics and flame was investigated in a high pressure combustor up to 5 bar, using high-speed diagnostics [22]. While these studies have provided considerable insight into the physical mechanisms governing swirling spray combustion, the design, power and operating conditions relative to the fuel injection system are generally far different from industrial aeronautical combustion systems. It is therefore crucial to better understand the underlying physical and chemical processes in order to optimize the architecture of future aircraft fuel injection systems. This involves performing detailed experiments on relevant swirl-stabilized spray flames so as to improve the industrial aircraft engine performances.

The current paper deals with a detailed experimental study of an advanced helicopter LP fuel injection system operating at atmospheric pressure in an optically accessible GT model combustor. This injector is fuelled with commercial Jet-A1 fuel and preheated air. In a first step, various experiments using laser diagnostics were performed. First of all, the aerodynamic conditions were investigated using high-speed PIV and stereoscopic PIV laser diagnostics. Experiments on the characterization of the flame structure were pursued with OH-PLIF operating at low frequency. Finally, the dynamics of flame structure/flow field interactions were investigated thanks to the combination of high-speed OH-PLIF and PIV techniques. From the analysis of the velocity measurements, the distributions of the averaged 2D flow velocity as well as information about the strain rate and vorticity distributions provided an overview of the aerodynamic flow field. In particular, the results illustrated the mechanisms of generation of the shear layers and their effects on the flame front. A specific tool was developed in the current study to extract the accurate flame front position via the analysis of the OH gradient. An analysis of the experimental high-speed velocity data was then performed with a Proper Orthogonal Decomposition (POD) tool to obtain a detailed description of the dynamics of the aerodynamic flow. Finally, a careful analysis of high-speed flow velocity and POD analysis combined with OH

distributions was used to study the formation of unusual flame pinching mechanisms and their effects on the transporting of unburned pockets into the burned gases.

2 Experimental set-up

2.1 Combustion facility and operating conditions

A visualization of the experimental facility is given in

Fig. 1. The mono-sector gas turbine combustor is composed of two parts, the combustion chamber and the fuel injection system (Fig. 1a). The combustion chamber is the same as the one described in [23]. It has a square cross-section of 100 mm × 100 mm and a height of 230 mm. It is equipped with three UV fused-silica windows that guarantee large optical access (80 × 200 mm^2). The exhaust opens directly on the ambient air with a 56 mm diameter nozzle. The LP fuel injection system is located at the bottom of the combustion chamber and fuelled with commercial liquid Jet A1 fuel. Air is fully injected into the fuel injector and acts as a promoter to atomize the liquid fuel. The LP injection system is based on a premixing of air with a liquid spray fuel issued from a fuel nozzle and a thin liquid film produced along the wall of the injection system. A schematic of the LP fuel injection is depicted in Fig. 1b. The injection system includes two co-rotating swirlers and a hollow cone central fuel injector. The central swirl air flow is radial while the one used for the outer annular air flow is axial. The liquid fuel is injected via two channels. The main injection circuit consists of the radial injection of kerosene to the radial swirl air through eight radial holes of diameter 1 mm staggered in two rows. A hole drilled along the fuel nozzle with an internal diameter of 1 mm, constitutes the pilot injection. This one is used to axially inject the remaining kerosene in the air stream. The atomization of the liquid fuel injected through the main injection system is similar to the one obtained from the injection of a liquid jet in a cross-flow. Radial kerosene jets are destabilized by the axial swirl air stream, resulting in jet breaks and droplet formations. According to the geometry of the injector, the larger "inertial" fuel droplets also impact the wall of the external tube of the central flow, thus forming a thin liquid film. This one is then atomized through the action of the external swirl air flow which provides a shear force resulting from the interaction of the free liquid surface with an airflow stream. This interaction forces the liquid film to move towards the lip of the pre-filmer where the axial swirl air stream deforms its

edge and leads to the disintegration of the liquid film in form of ligaments and then to small droplets as schematically shown in Fig. 1b. Finally, the axial swirl air stream thus makes it possible to homogenize the mixture between air and fuel at the outlet of the injector. Finally, the pilot injection system enables to produce a rich zone in the center of the flow to promote the stabilization of the flame at the outlet of the injector.

The exit plane of the fuel injector is located in the bottom plane of the combustion chamber (z/D = 0). The operating condition investigated in the current study delivers a thermal power of 65.6 kW, with a global equivalence ratio of ϕ= 0.7, $\dot{m}_{air}$ = 30 g/s and $\dot{m}_{fuel}$ = 1.417 g/s. In order to ensure operating conditions representative of those encountered in industrial gas turbines, the air inlet at the entrance of the combustion chamber is preheated to 473 K. The flame stability is controlled by the analysis of the pressure fluctuations measured inside the combustion chamber with a pressure transducer.

2.2 Laser diagnostics

Two regions of interest were considered in the current study (Fig. 2). The first one allows measurements of velocity in a cross section of the reactive flow field (Fig. 2a) while the second one was used to perform measurements of velocity and OH distributions in the axial plane centred along the flow axis (Fig. 2b). These measurements were performed with a variety of PLIF and PIV diagnostics. The size of the regions investigated as well as the associated spatial resolution selected for PIV and OH-PLIF measurements are reported in Table 1.

2.2.1 PIV systems

Two PIV systems were used to perform 2D axial (x-z plane) and radial (x-y plane) measurements of velocity. For measurements in the radial plane, a stereoscopic PIV system was used. A schematic representation of the experimental setup is given in

Fig. 2a. The PIV system consisted of a dual-cavity Q-switched Nd:YAG laser running at 5 Hz and providing two 532 nm laser pulses with a pulse timing separation of 2 µs. The laser beam was formed into a 70 mm tall planar light sheet using a cylindrical telescope (f_1 = - 20 mm, f_2 = 500 mm) and focused to a waist of 500 µm using a spherical

lens (f = 1000 mm). Mie scattering produced from the illumination of solid zirconium oxide (ZrO_2) particles of several μm nominal diameter seeded into the flow and kerosene droplets by the laser beam were detected and imaged using visible cameras (Dantec Dynamics FlowSense 4M). To minimize the scattered light from kerosene droplets, the laser sheet was located at a minimal distance of 25 mm downstream from the exit of the injection system in which the sizes of ZrO_2 particles and fuel droplets had typically the same order of magnitude. The cameras operated with a 2048 × 2048 pixel resolution. For each camera, a Nikkor f/1.2 50 mm lens was mounted with a Scheimpflug mount tilted with an angle of 35°. A narrowband optical filter centred at 532 nm with a 10 nm spectral width was placed in front of the lens in order to suppress the background flame luminosity. Calibration of cameras was performed to correct the perspective distortion and images were then de-warped and cross-correlated to extract velocity fields using the commercial, multi-pass adaptive window cross-correlation software (Dynamics Studio) developed by Dantec. A final interrogation window size of 64 × 64 pixels with a 50% overlap was obtained. The resulting horizontal plane section analysed in the flow was a section of 60 × 70 mm^2 at 25 mm above the burner exit. This corresponded to 177 × 149 vectors, and a vector spacing of 0.46 mm.

For velocity measurements in the stream-wise direction, high-speed PIV experiments were conducted to study the flow dynamics. The laser system consisted of a double cavity Nd:YLF laser, DarwinDual, Quantronix operating at 5 kHz, with pulse energies of 6 mJ/pulse. The signal was collected with a CMOS high-speed camera (Photron SA1.1) equipped with a Nikkor 80 mm lens (f/1.4) and an optical band-pass filter centred at 532 nm. The camera was a 8-bit, 1024 × 1024 pixel imaging array (20 μm square pixels) able to acquire images at a frame-rate up to 5400 fps in the full frame mode. Operating at 5 kHz, the array size was optimized to 768 × 768 pixels and images were post-processed with the commercial Dynamics Studio software. A multi-pass adaptive window cross-correlation with a final interrogation window size of 16 × 16 pixels and a 50% overlap was used. No data filtering was performed on the PIV measurements, only spurious vectors were suppressed. The field of view observed in the flame extended from z/D= 1 to z/D=3 and was 76 mm large, with a vector spacing of 0.63 mm.

2.2.2 OH-PLIF systems

Two OH-PLIF acquisition systems were used to characterize the flame structure. A conventional OH-PLIF system delivering laser pulses with high energy was initially

used to acquire OH fluorescence images at low frequency (3.33 Hz) with a large signal-to-noise ratio. The region of the flame observed with the laser sheet was 60 mm from the exit of the injection system and 80 mm along the cross-section of the combustion chamber. A Nd-YAG laser operating at 532 nm was used to pump a tuneable dye laser (Quantel TDL90) supplied with Rhodamine 590 dye. The thickness of the laser sheet was about 150 µm and the resulting output pulse energy at the probe volume was fixed to 20 mJ. The excitation wavelength was tuned to 282.75 nm corresponding to the spectral location of the $Q_1(5)$ rotational transition of the $A^2\Sigma^+(0,0) \leftarrow X^2\Pi(0,1)$ electronic band. The detection system consisted of an Em-ICCD camera (PIMAX4) mounted with a 100 mm, f/2.8 UV-objective (Cerco). A combination of optical filters allowing the detection of fluorescence signals over a spectral band centred at 310 nm with a 30 nm spectral width was used. This strategy enables a significant reduction of possible crosstalk between OH fluorescence and mono- and di-aromatics fluorescence contained in kerosene via the following combined effects: 1/ the use of an excitation wavelength of 282.75 nm reduces significantly the fluorescence of mono-aromatics in the spectral OH fluorescence collection domain [24, 25]; 2/ performing fluorescence measurements on OH with a linear regime of fluorescence reduces the intensity of the excitation laser beam. Therefore, the intensity of kerosene fluorescence can be largely decreased while the optimization of the OH fluorescence is maintained; 3/the use of a narrow band-pass filter for OH detection allows to record a small extent of the broadband kerosene fluorescence. To ensure that the kerosene fluorescence interference is negligible in our current study, an experiment was carried out by slightly detuning the frequency of the excitation laser beam to guarantee no excitation of an OH rotational transition while continuing to promote an excitation of kerosene. Results showed that the kerosene fluorescence signal collected onto the camera was comparable to the noise signal of the camera, demonstrating that the kerosene fluorescence is negligible in our operating conditions when recording the OH-PLIF images. Furthermore, elastic light scattered by particles and fuel droplets into the flow was suppressed using a high transmission Schott WG295 filter coupled to a band-pass Schott UG11 filter. Laser sheet energy distribution was finally measured by filling the combustion chamber with acetone vapour before the experiment and by recording an averaged acetone fluorescence image obtained from the data processing of 1000 single-shot acetone-PLIF images.

The shape and dynamics of the flame were analysed with a high-speed OH-PLIF system. A schematic representation of the experimental setup is given in

Fig. 2b. The high-speed OH-PLIF system consisted of an Nd-YAG laser operating at 527 nm, generating laser pulses at a repetition rate of 10 kHz and delivering an average power of 105 W. The resulting green laser pulses pumped a tuneable dye laser (Sirah Credo with a mixing of Rhodamine 590 and ethanol) that produced at 10 kHz ~ 350 $\mu J/pulse$ with a 20 ns pulse duration. The laser wavelength was tuned to the $Q_1(5)$ rotational line. This wavelength was controlled using OH fluorescence signals recorded in a laminar CH_4/air flame. The UV laser beam was superimposed with the PIV laser beams, using a dichroic mirror and was expanded through a set of fused silica lenses ($f_1 = 1000\ mm, f_2 = -20\ mm, f_3 = 500\ mm$) to form a 50 mm tall planar light sheet. OH fluorescence signals were collected with an intensifier (High-Speed IRO, LaVision) coupled with a high-frame rate CMOS camera (Fastcam SA5) operating with a 896 × 848 pixel resolution. A 100 mm, $f/2$ UV objective lens (B. Halle Nachfl. GmbH) was mounted on a Scheimpflug mount to ensure a camera tilt angle of 27.5° (

Fig. 2b). The filters used in the high-speed OH-PLIF measurements were the same ones used in the low repetition rate PLIF measurements.

2.3 Image Data Processing

2.3.1 OH-PLIF image filtering and flame front detection

Once the OH fluorescence images has been corrected from the distortion and spatial energy distribution of the laser sheet, a filtering procedure was applied to detect the flame front contour. In many studies, linear diffusion filtering using Gaussian routines is applied to reduce noise before extracting the flame contour. However, this type of filtering generally smoothes the noise but blurs important features such as the edges and thus makes them harder to identify [26]. To limit these constraints, non-linear diffusion filtering routines are used to improve the Signal to Noise Ratio (SNR) while enhancing the contours in images [9,27,28]. This procedure offers the advantage of locally modifying the diffusion coefficient according to the type of object observed on

the images. Thus, a large diffusion coefficient can be used to smooth the noise while a negligible one is applied when approaching to the object boundaries. As a result, flame contours can be enhanced, gradients are sharpened and detection of the boundaries is highlighted. The non-linear diffusion method used in the current study then solves the following partial differential equation (PDE):

$$\frac{\partial u}{\partial t} = div(g(|\nabla u|^2)\nabla u) \quad (1)$$

in which g is a diffusivity function and u(t, x, y) is the OH fluorescence signal on the image. Considering that the edges of the object are detected by the gradient of u, $|\nabla u|^2$, a diffusivity function $g(|\nabla u|^2)$ can be introduced by using the formalism proposed by Perona and Malik [29]:

$$g(|\nabla u|^2) = \frac{1}{1 + \left(\frac{|\nabla u|}{\lambda}\right)^2} \quad (2)$$

where λ is defined as a contrast parameter. With this expression, only gradient intensity values lower than λ are diffused. To provide a better converging effect of averaging the gradient within the diffusivity, the diffusivity function $g(|\nabla u|^2)$ proposed by Perona and Malik was replaced by the expression $g(|\nabla u_\sigma|^2)$ with $u_\sigma = K_\sigma u$ and K_σ denoting a Gaussian function with a standard deviation σ. The numerical implantation of this filtering method was achieved by discretizing the PDE equation with an iterative process. The simplest procedure consisted in the use of an explicit scheme, but for stability reasons, this method is severely restricted to very small time steps, leading to a high time cost. A solution to circumvent this constraint was to use the additive operator splitting (AOS) method proposed by [26]. Using a semi-implicit scheme, the computational cost was then increased compared to the case of the explicit scheme but time steps are no longer limited. Thus, the global computation time is reduced. To illustrate the potential of this filtering method, the instantaneous profiles of the OH signal intensity at z/D = 2 from the raw OH images and the filtered OH images are plotted in

Fig. 3a. One can observe that the noise is smoothed by the filtering tool (green line) while the sharp gradients of OH signals are well preserved. To isolate the sharp

gradients, filtered OH images were converted into binary images with black regions corresponding to fresh gas and gray to white zones denoting the burned gases. The threshold limit adopted for this binary conversion was defined using Otsu's method [30]. The frontier separating both the two zones was then defined. The advantage of this method is highlighted in

Fig. 3b in which the OH flame contours deduced from non-filtered and filtered instantaneous OH fluorescence images are compared. It can be seen that the detection contour based on the Otsu's method on non-filtered OH images fails in regions with low SNR (red lines at the top of Fig 3b). Indeed, the application of the Otsu's method on weak signals in which gradients are difficult to isolate does not significantly reduce the blurring at edges. On the contrary, the filtered OH image enhances the contrast of the OH signals, this enabling unambiguous detection of the contour between the burned gases and fresh gases.

2.3.2 Proper Orthogonal Decomposition analysis

The Proper Orthogonal Decomposition (POD) is a statistical tool for identifying and extracting coherent structures and energetic events in flows. POD consists in the determination of a set of bases of linear functions, the so-called proper orthogonal modes which contribute most of the energy of the flow. The approach selected in the current study is based on the snapshots method introduced by [31]. POD reconstruction is used as a low-pass filtering to remove small velocity fluctuations and enable identification of the most energetic coherent structures that cannot be clearly observed on the raw experimental velocity fields [32]. To illustrate the potentialities of POD on realistic reactive flows, it was applied on the velocity field measured in a focused region of interest (i.e. on the left side of the flow since the flame is assumed to be symmetrical). 3750 instantaneous velocity fields recorded at 5 kHz were used. A typical comparison of the POD reconstruction of the fluctuation energy (

Fig. 4b) with the experimental vorticity (

Fig. 4a) is displayed. By using only 50 modes which accounts for 70% of the energy of the fluctuations, the POD reconstruction enables the position and intensity of the experimental vorticity to be captured.

3 Results and discussion

3.1 Averaged velocity field

A set of 3750 instantaneous velocity fields was used to compute time-averaged statistics with a good convergence. The mean flow field was found to be axisymmetric. To illustrate the main properties of the time-averaged flow pattern,

Fig. 5 displays a streamline plot superimposed on the mean velocity flow (Fig. 5a) and the turbulence kinetic energy (TKE) fields (Fig. 5b). In the current study, TKE was calculated as $\frac{1}{2}\sum_i u_i' u_i'$ in which u_i' is the fluctuation of the velocity component in the direction i (x, y or z). Since only the axial and radial velocity components are measured, the out of plane velocity fluctuations are assumed to be equal to the radial fluctuations for the calculation of TKE.

The averaged flow velocity is typical of those observable in enclosed swirled flames [9,33]. The air/fuel fresh mixture expands downstream from the injector along a conical spatial distribution with a magnitude of axial velocity that may exceed 150 m/s. The geometry of this flow, in a time-averaged approach, consists of several main regions: a large inner recirculation zone (IRZ) that is developed through the positive axial pressure gradient associated with the vortex breakdown of the swirling flow, an outer recirculation zone (ORZ), a toroidal recirculating region generated by the rapid expansion of the nozzle in the combustor, an annular jet flow at elevated velocity that separates these two regions and two annular shear layers that divide the ORZ and the jet inner flow, and IRZ and inner flow, denoted here as the outer shear layer (OSL) and the inner shear layer (ISL). Each shear layer originates from the existence of a large velocity gradients between the inner flow and the recirculation flows, thus generating

strong velocity fluctuations. Analysing the RMS of the velocity (Fig. 6), the highest velocity fluctuation is produced in ISL for the axial component (Fig. 6b) and in OSL for the radial component (Fig. 6a). It can be noted that the fluctuations associated with ISL are two times larger than that of OSL. To complete the description of the turbulence of the flow field, large turbulent scale structures are also observable on the instantaneous 2D flow velocity displayed in Fig 7. These ones are mainly located in the ISL and OSL regions, zones in which mixing between fresh gases and hot products is highly promoted.

Radial velocity flow components were also measured by using stereo-PIV in a cross-section perpendicular to the flow axis. The streamlines of the averaged flow velocity, coloured by the axial flow velocity and the associated TKE are presented in Fig. 8a. Results were obtained from the data processing of 250 instantaneous 2D flow velocities recorded at z/D= 1.1. As expected, results demonstrated that the averaged velocity flow and TKE distributions are axisymmetric. The radial profiles (x/D= 0) of the average and RMS values of the three velocity components are also reported in Fig. 8b. Measurements show that the flow velocity field presents a high three-dimensional feature since tangential and radial velocity components are of the same order of magnitude. The tangential velocity u_y in the ORZ is around 30% larger than the radial velocity u_x. On the contrary, the radial velocity component displays a larger value compared to the tangential velocity in the inner flow, in which axial velocity is maximal. This difference of behavior in IRZ and the inner flow highlights the large velocity gradients in ISL.

Based on experimental knowledge of the three components of the velocity flow, the aerodynamic Swirl number at z/D = 1.1 was calculated using the following relation:

$$S = \frac{\int_0^R \rho . u_\theta . u_z . 2\pi r^2 . dr}{R_{inj} \int_0^R \rho . (p + u_z^2) . 2\pi r . dr} \quad (3)$$

The pressure effect is usually neglected in experimental studies since it is difficult to obtain. The quantities u_z and u_θ stand for the axial and azimuthal velocities at the outlet of the injection system. Pressure and density effects are neglected in the calculation. A value of S = 0.62 was calculated assuming a characteristic length equal

to the radius of the nozzle exit R_{inj} and an integration domain ranging from x/D = 0 to 1.3. The existence of a high degree of swirl (larger than 0.62 at the exit of the fuel injection system) confirms the experimental results, namely that an axial recirculation bubble in the form of a central toroidal recirculation zone occurs in this type of flame.

3.2 Strain rate and vorticity

The 2D flow velocity distribution from PIV measurements was used for a direct calculation of gradient-based quantities such as the strain tensor and vorticity. These quantities provide a useful basis for the analysis of the non-linear coupling between turbulence and chemical processes leading to a wrinkling and a straining of flames. The strain tensor in the x-z plane was obtained from the following expression:

$$S_{xz} = \frac{1}{2}\left(\frac{\partial u_x}{\partial z} + \frac{\partial u_z}{\partial x}\right) \tag{4}$$

in which the quantity u_i denotes the turbulent velocity in the direction x_i. The out-of-plane component of vorticity (ω_y) was computed using the curl of the velocity field. For a planar 2D flow velocity field, the out-of-plane vorticity is computed as

$$\omega_y = \frac{\partial u_z}{\partial x} - \frac{\partial u_x}{\partial z} \tag{5}$$

Fig.9a presents the mean strain rate component in the x-z (measurement) plane. Maximum values of the strain rates (regardless of its sign) occur at the interfaces between the inlet flow and each recirculation zone (ORZ and IRZ). More remarkably, the thicknesses of the two shear layers differ among themselves.

In an open channel sudden expansion, the main stream separates from the corner of the expansion and reattaches downstream. The separating streamline is thus defined as the frontier between the main inlet stream issued from the injection system and the ORZ. One specificity of the ORZ is its low velocity magnitude compared to the inlet stream. Consequently, the separation streamline is representative of high turbulent mixing layers with presence of large velocity gradients. The growth rate of the mixing layer is then generally piloted by the Kelvin-Helmholtz instability mechanism [31]. Even for high Reynolds numbers (up to 200 000), Kelvin-Helmholtz instability generates primarily two-dimensional, spanwise-oriented vortices (rollers) that are transported downstream with a convective velocity function of the free stream speed

ratio r=U_2/U_1. The velocity with the subscript "2" is associated with the low speed of the positive stream-wise developed in the ORZ and the velocity with the subscript "1" refers to the high-speed inlet stream. For incompressible mixing layers, the growth rate of the shear layer driven by the Kelvin-Helmholtz mode can be then expressed as a function of the velocity ratio (r) and the density ratio ($s = \rho_2/\rho_1$) by the following expression [34]:

$$\frac{\delta}{z} = 0.17\frac{(1-r)\left(1+\sqrt{s}\right)}{\left(1+r\sqrt{s}\right)} \quad (6)$$

δ is the visual thickness of the shear layer and z is the downstream distance from the corner of the outlet wall of the injector. In our case, assuming U_1 = 120 m/s, U_2 = 30 m/s and a density ratio of 1/5 (ratio of temperature between the hot gases contained in the recirculation zone and those of the inlet jet), the value of the thickness is calculated for different heights above the burner and plotted on Fig. 9b. The evolution of the theoretical thicknesses versus the height is then compared to the experimental values measured in the shear layers. For instance, at z/D=1.1, the theoretical thickness is about 4.1 mm which agrees well with the experimental value of 4.4 mm acquired in the ORZ. By contrast, the thickness observed experimentally in the ISL is noticeably larger, around 9 mm. This value is apparently too large to originate from the development of the ISL by only Kelvin-Helmholtz instabilities. As IRZ is not attached to the injection system (i.e. no existence of a bluff body at the center of the outlet injection system), the ISL is no longer driven solely by Kelvin-Helmholtz instabilities but is likely piloted by another mechanisms that also produce smaller-scale, streamwise-oriented vortices lying along the outer edges of the spanwise rollers and grouping in counter-rotating pairs. According to the literature [35], one possible mechanism could be related to the sudden increase in three-dimensionality and the accompanying increase in the amount of molecularly-mixed fluid associated with the mixing transition. Therefore, the existence of highly turbulent motions inside the inlet flow (see Fig. 5) are key parameters which enable the strain and the distortion of the volume of hot exhaust gases circulating in IRZ, breaking then the interfacial zone between the main flow and the reverse flow in the IRZ into smaller volumes and accelerating an homogenization of the mixing layer in a larger section. Thus, the mixing taking place along the interface between the inlet stream and the hot gases circulating inside the IRZ is more efficient and provides a favorable zone for the ignition of the incoming fresh gases and flame stabilization, compared to the OSL (see

section 3.3). A second instability mechanism which could explain the thickness of the ISL is the presence of a precessing vortex core (PVC). Indeed, formation of the IRZ may be accompanied by the occurrence of a PVC which strongly impacts the flame stability and may affect stretch and local quenching of the reactions zones [36]. However, no evidence of remaining PVC structures in the flow regions investigated can be found in PIV images and it is therefore difficult to assess the presence of PVC. Furthermore, oscillations in the flow field arising from the PVC (if any) would decay rather rapidly as the flow is propagating downstream from the injector [12,37]. Oscillation amplitudes would significantly decrease at axial distances from the breakdown corresponding to about one to two nozzle diameters. Considering an exit nozzle diameter of D ~ 2 cm, the effect of PVC is expected to be negligible in the IRZ where flame pinching effect is observed.

Positive and negative values of the shear strain rate observed in Fig. 9a also indicate two opposing directions of the fluid angular deformation inside the flow. For the left zone of the flowfield displayed in Fig. 9a, the positive values correspond to the OSL delimiting the zone between ORZ and the inlet flow while the negative values are representative of ISL. These opposite trends are easily explained by the orientation of the vortex structures generated at the interface between the recirculation zones and the inlet flow, which are counterclockwise for OSL and clockwise for ISL.

Fig. 10 displays the mean vorticity field $\overline{\omega_y}$ calculated from the average of 3750 instantaneous vorticity fields. To locate the high vorticity regions in the velocity flowfield, streamlines are added on vorticity maps. The vorticity field appears similar to the corresponding strain rate, which suggests a dominance of the axial-velocity-gradient term in Eqs. (4) and (5). Regions of positive and negative (red and blue) vorticity properly identify the counter-clockwise and clockwise rotating flows on the left hand side of the flowfield. A peak vorticity magnitude of more than 15 000 s^{-1} is observed in ISL and OSL. This high level of vorticity shows that intense mixing takes place between the input reactants and hot products circulating in the ORZ and IRZ and confirms the observations already observed on the strain rates. This intense mixing also promotes the heat transfer between the hot gases and the fresh incoming mixing required for the ignition and the burning of the fuel/air mixing penetrating into the shear layers (see the next section for more information).

3.3 Flame structure

Figure 11 shows the 2D distribution of the OH* chemiluminescence after an Abel transform downstream from the injector as well as the streamlines of the averaged 2D flow velocity. A false colormap directly correlated to the pixel signal intensity was applied to provide a visual representation of the location of the highest OH* intensity in the reaction zone, and thus indication of the localization of heat release. Therefore, the time-averaged OH* distribution shows a rather V-shape flame with a central region of heat release located between z/D = 0.2 and z/D = 2.7.

Typical instantaneous OH fluorescence images corrected from the energy distribution of the laser sheet and the background noise are displayed in Fig. 12, enabling an overall description of the flame topology. In general, the high level of velocity fluctuations in such swirl spray flames causes an oscillation of the flame which surges back and forth axially between two specific combustion regimes. The first one corresponds to the case of the generation of an inner flame that is anchored to the fuel spray (i.e. a few mm from the exit of the injection system) while the second combustion regime delivers a flame that is lifted far away from the top of fuel spray (i.e. z/D = ~ 1), spreading the flame over large horizontal distances (Fig. 12a-b). Between these two combustion regimes, the base of the inner flame oscillates between these two extreme positions (Fig. 12c). A temporal analysis of successive OH-PLIF images reveals that the reactive flow is prone to sporadic oscillations and not to periodic instabilities. Apart from the temporal variations of the inner flame position, the flow/flame mechanisms generating these flames deliver similar combustion performances whatever the regime investigated.

In the first combustion mode, the instantaneous OH-PLIF image displayed in Fig. 13a enables a detailed description of the flame topology that emanates from various flame/flowfield interactions. The dark zone defined as (A) on the OH-PLIF image corresponds to the entrainment under elevated velocity of the fresh air/fuel mixing downstream from the injector. At the bottom of this region, the detection of strong Mie scattering signals as well as intense kerosene fluorescence signals denotes the presence of fuel droplets spreading along a hollow cone shape with an angle of 45° with respect to the combustor inlet plane (zone B). Mixing of fuel droplets and fuel vapour with air along the streamwise direction then promotes the generation of the inner flame located

at the top of the fuel spray (zone C). The inner flame is quite straight over a distance of z/D= 1.3 before being suddenly expanding into the combustion chamber under the action of the vortex breakdown bubble (zone D). In zone D, the OH radicals that are produced in the flame front are transported away by convection and molecular diffusion and are subsisting due to favourable elevated temperature conditions in IRZ. At elevated temperatures, the lifetime of OH radicals is quite long (up to 3 ms), thus enabling them to be transported along large distances (typically ~ 15 cm for a velocity of ~50 m/s) [38]. Part of the combustion products circulating in IRZ is also transported into the outer recirculation zone (ORZ) formed at the intersection of the inlet plane of the burner and the walls (zone E). Furthermore, ORZ is fed with OH radicals issued from OSL. These results are well supported from the OH* chemiluminescence distribution displayed in Fig.11. It is thus confirmed that the heat release region, i.e. the zone of OH* chemiluminescence is limited only up to a height of z/D= 2.0 (along the flame axis), demonstrating that the OH fluorescence signals detected above this value are produced from hot products of combustion and not from OH molecules produced into the reaction zones.

As noted on both instantaneous OH-PLIF images, the edge zones delimiting the interface between the fresh gases and the reverse flows (i.e. ORZ and IRZ) are highly wrinkled. However, a careful examination of Fig. 13a shows that OSL and ISL display reactive flow structures with different scales. The prevailing inner flame structures are noticeably smaller than those observed in OSL. These apparent differences arise from the reasons already mentioned to explain the existence of dissimilar shear layers. In the case of the inner flame, the intense level of turbulence in ISL leads to an enhancement of the transport of fresh air/fuel gaseous pockets within the flame front by small size eddies that can easily penetrate into IRZ. As a result, the fresh gaseous mixture contained in these eddies is preheated and mixed with radicals faster, enhancing the reaction rates as shown by the large production of OH radicals in this region (Fig. 13a). Returning to OSL, the structure of the interface delimiting ORZ and the inner flow is also prone to similar physical mechanisms. However, the burning of the fresh incoming reactants seems to be reduced. As observed in Fig. 13a, the fluorescence intensity delivered by the OH radicals in ORZ is significantly lower than the one issued from OH radicals in the inner flame. Furthermore, the structures of the hot/fresh gas interface are now tightly rolled-up by large-scale eddies caused by the Kelvin-Helmholtz instability developed at the outer corner of the injection system.

These large-scale vortices result in curvature induced stretch flames which unfortunately hamper the efficient mixing between fresh reactants and combustion products. Furthermore, the heat transfer between the combustion products circulating in ORZ and the combustor walls leads to large heat losses that significantly reduce the local temperature of hot gas products, see for example the work of Mercier et al. on this subject [39]. Under these conditions, the reactivity of the fresh mixture upstream of the interface is then reduced to such a low level that the flame leading edge can ultimately lead to flame extinction. The frontier observed experimentally may be only characteristic of an interface between hot combustion products and fresh incoming reactants and not that of a flame front. To support these assumptions, the progress rate of combustion in the two shear layers was determined by extracting the gradient of the OH fluorescence signals from instantaneous OH-PLIF images. A recent study revealed that OH-gradients related to strong temperature gradients and/or presence of OH in superequilibrium conditions can be a good marker of the flame front of swirl flames [38]. In the current study, the intensity distributions of the OH-gradients in ISL and OSL were deduced from the post-processing of instantaneous OH-PLIF images. This post-processing consists of the detection of the OH-gradient using Sobel filtering followed by thresholding the gradient and "cleaning" residual small structures by a morphological operation [40]. The threshold limit was fixed at 15 % of the maximum gradient intensity to remove weak values of OH-gradient signals in regions with weak SNR.

The OH-gradient image shown in Fig. 13b and calculated from the instantaneous OH-PLIF image plotted in Fig. 13a displays the distribution of the local reaction rates inside the flame. Typically, the reaction rates produced in such flames are localized inside the heat release region already observed in Fig. 11. An examination of both distributions (see Fig. 11 and Fig. 13b) enables to find strong correlations between the frontiers delimiting the reaction zones and the regions of hot combustion products. For instance, the lower frontier observed on the OH* chemiluminescence distribution corresponds to the reaction zone delimiting ORZ (E) and the fresh air/fuel mixing zone downstream from the injector (A) while the upper frontier visualizes the reaction zone existing between the luminous zone corresponding to the expansion zone of the flame (IRZ) and the hot combustion products region (D). A careful observation of Fig. 13b also highlighted the identification of other reaction zones that could not distinguish in Fig.11. Indeed, it can be seen that the most intense reaction zone occurs at the edge

between zones A and C, confirming the production of a thin flame front in ISL. On the other hand, the OH-gradient intensities in the zone delimiting regions E and A are significantly weaker. This result suggests that the modification of the flame stretch in OSL, a combination effect of the net increase of the strain rate and flame curvature, modifies the burning velocity and creates favourable conditions to reduce the reaction rates which ultimately lead to local flame extinction. Therefore, the reactant mixture that should have been consumed in OSL is then transported downstream, causing a potential source of pollution by the release of unburned products into the exhaust gases. To support this trend, an inspection of the red box referencing part of zone F in Fig. 13a clearly confirms the presence of isolated pockets of unburned gases downstream from the incoming jet flow (around x/D = - 1.1 and z/D greater than 2.5). An inspection of the literature shows that the propagation of unburned mixtures in the exhaust products is a physical process already observed in academic turbulent premixed flames classified in the corrugated-flamelet regime [41–46]. Their origin has been attributed to the engulfment of coherent structures in the flame front due to high levels of turbulence and their resulting sizes were estimated to be equal to or larger than the integral length of turbulence [43]. Results from DNS simulations on a turbulent premixed H_2-air flame also revealed that these isolated pockets are three-dimensionally connected to the unburned zone by a flame structure called "handgrip" [47]. This three-dimensional handgrip structure was confirmed experimentally in the case of relatively high Reynolds number turbulent jet premixed flames [45]. The flow structure and the occurrence of a pair of counter-rotating vortices from either side of the incoming jet interacting with the flame front were responsible for the pinch-off of the flame, leading to the generation of unburned pockets. It is worth noting that this mechanism was numerically studied for academic gaseous premixed flame [48,49] and spray flame configurations by [50]. It was demonstrated that vortices with sufficient intensity can pass through the flame front and remove an oxidizer pocket on the spray side.

However to the best of our knowledge, no detailed experimental data are available to understand the flame-flow interactions leading to the penetration of such large-scale unburned pockets into the exhaust gases. To overcome this lack of information, their surface was initially estimated by the data processing tool already described and used to determine the flame contour. Assuming that the unburned pockets are three-dimensional, an average diameter of 9 mm with a standard deviation of 3.9 mm was

estimated. This diameter is comparable to the integral length scale of 11 mm that was obtained from the data processing of the instantaneous 2D velocity fields.

To gain deeper insight into the formation of unburned pockets in IRZ, the dynamics of formation of these unburned pockets was then experimentally investigated by performing time-evolving combined OH-PLIF and PIV measurements. All the results of these experiments are now detailed in the next section.

3.4 Dynamics of flame/flow interactions

Experiments were focused in a region located between z/D=1 and z/D=2.5 in which flame pinching phenomena with similar time evolutions are often observed. To illustrate their mechanism of formation, Fig.14 displays successive instantaneous OH-PLIF images recorded with a time interval of 0.1 ms. The OH-PLIF images presented in Fig. 14a-d are superimposed with the streamlines obtained from high-speed PIV measurements. Complementary to these data, Fig. 14e-f shows the vorticity fields deduced from the POD filtering of the instantaneous flow velocity distributions recorded at 5 kHz as well as their associated streamlines. The interface separating the fresh gases from the burnt gases was calculated using the processing tool detailed in section 2.3.1 and results are plotted on each image. Analysis of the time evolution of the flame pinching starts at the reference time t = 0 ms (Fig. 14a). This physical process is initiated when the fresh reactants transported at high velocity impact the lower part of IRZ. As supported by the large OH signals detected in Fig. 14a, the reaction zone is mainly located on the right side of the reactant jet and to a lesser extent on the upper part of the incoming reactant jet. Furthermore, the vorticity map (Fig. 14e) calculated from the velocity field displayed in Fig.14a highlights islands of large vorticity that reveals the location of counter-rotating vortices between the reactants and the burnt gases circulating in IRZ. These vortices shown schematically on Fig.14e contribute then to the production of SL along the contours of the reaction jet. At t = 0.1 ms, both sides of the reactant jet are slightly tightened by the stretching and the movement in opposite directions of vortices. The reaction zone is still maintained on the right side of the reactant jet (Fig. 14b). The velocity field recorded at t = 0.2 ms (Fig. 14c) and the POD-reconstructed vorticity fields (Fig. 14f) indicates that the two vortices are convected further downstream, rapidly pushing part of the reactants into the burnt gas region. At the same time, a careful examination of the POD-reconstructed vorticity field image (Fig. 14f) also indicates the emergence of a second set of vortices on the left and right edges of the reactant jet, thus deflecting the streamlines in the bottom part of

the investigated region. At t=0.3 ms (Fig. 14d), these effects, combined with a stretch generated by the vortices cause a separation of a large pocket of reactants from the bulk of the fresh gases. This pocket is then convected and diluted at high velocity through the burnt gases without burning. On the contrary, the reaction zone on the right side continued and even intensified since the roll-up of the flame front induced by vortices enables larger strain rates; the reaction rate is then intensified following the convection and diffusion of the reactants through the flame front. This effect makes it effective the penetration of the reactant flow through the braid of the vortex, offering physical conditions similar to those encountered in the vicinity of a stagnation point. In particular, as the velocity of the reactants is nearly equal to zero, the heat release transferred to the reactants by hot gases through the roll-up in the vortex is then significantly increased, giving rise to favourable conditions for their ignition [14].

This investigation of the flame splitting is partial, since the out of plane component of velocity is unknown, making it impossible to accurately evaluate the gradient in the third direction. However, as demonstrated in the current study, for most of the time-series of measurements, it is possible to track the temporal evolution of the flame front and an analysis of these data reveals in many occasions this sequence of flame pinching, consolidating then this analysis.

4 Conclusions

A gas turbine model combustor equipped with an industrial lean premixed fuel injection system and supplied by liquid kerosene was experimentally investigated. Non-intrusive laser diagnostics were applied in operating conditions representative of the ones encountered in real aeronautic propulsion systems, i.e. with a high swirl number (larger than 0.62 in the current study) and elevated inlet fresh gas velocities (~ 120 m/s). First, the interaction between the flame structure and the aerodynamic conditions were studied by PIV and OH-PLIF. The mean velocity and the flame shape distributions are typical of those encountered in confined swirled flames with the production of intense outer recirculation zones located on the corners of the combustion chamber and an inner recirculation zone located at the center of the reactive flowfield. This inner zone contributes to stabilizing the flame by the transporting hot products to the base of the fuel spray. Data processing of the strain rate and vorticity fields highlighted the existence of two shear layers that interfere differently with the inlet air/fuel mixing jet. The inner shear layer between IRZ and

the fresh inlet flow that is not anchored to the injection system is developed at the upper base of the fuel spray. The growth rate of the shear layer is then governed by the high level of turbulence that promotes, over a large three-dimensional zone the mixing of the fresh incoming products with hot products circulating in IRZ. The existence of a good mixing with a high level of local temperature in ISL provide favorable ignition conditions as well as the production of a flame front with an intense chemical reaction as noted from the large OH-gradient signals measured. On the contrary, the shear layer located between ORZ and the fresh incoming flow is mainly governed by a Kelvin-Helmholtz instability mechanism. This shear layer, anchored on the external corner of the injection system, develops spanwise-oriented vortices with a growth rate as a function of the free stream speed ratio (fresh incoming reactants and the flow circulating inside the ORZ). Data processing of the OH-PLIF images into OH-gradient distributions shows that these structures result in curvature induced stretch flames that reduce the mixing between the fresh reactants and combustion products. Added to this, heat transfer between the combustion products circulating in ORZ and the combustor walls also leads to significant heat losses that reduce the local temperature and hence the burning of the fresh gases close to the ORZ frontier. Consequently, the flame front developed in OSL is most commonly quenched. A careful analysis of high-speed flow velocity and POD results combined with high-speed OH distributions showed unusual flame pinching mechanisms leading to the release of subsequent unburned pockets propagating in the burned gases.

5 Acknowledgements

The authors are grateful for the financial support of the French aircraft motorist SAFRAN and the French National Research Agency (Industrial Chair PERCEVAL ANR-15-CHIN-0001). We also thank Benjamin Quevreux and Félix Frindt for their technical support.

References

[1] S.M. Correa, A review of NOx formation under gas-turbine combustion conditions, Combust. Sci. Technol. 87 (1993) 239–362.

[2] A.H. Lefebvre, D.R. Ballal, Gas turbine combustion: alternative fuels and emissions, in: Third Edit, Taylor & Francis, 2010.

[3] J. Janicka, A. Sadiki, M. Schäfer, C. Heeger, Flow and Combustion in Advanced Gas Turbine Combustion, Springer, 2013. doi:10.1007/978-94-007-5320-4.

[4] T.C. Lieuwen, V. Yang, Combustion Instabilities In Gas Turbine Engines, American Institute of Aeronautics and Astronautics, Reston , VA, 2006. doi:10.2514/4.866807.

[5] Y. Huang, V. Yang, Dynamics and stability of lean-premixed swirl-stabilized combustion, Prog. Energy Combust. Sci. 35 (2009) 293–364. doi:10.1016/j.pecs.2009.01.002.

[6] A.M. Steinberg, I. Boxx, M. Stöhr, C.D. Carter, W. Meier, Flow-flame interactions causing acoustically coupled heat release fluctuations in a thermo-acoustically unstable gas turbine model combustor, Combust. Flame. 157 (2010) 2250–2266. doi:10.1016/j.combustflame.2010.07.011.

[7] K. Oberleithner, M. Stöhr, S.H. Im, C.M. Arndt, A.M. Steinberg, Formation and flame-induced suppression of the precessing vortex core in a swirl combustor: Experiments and linear stability analysis, Combust. Flame. 162 (2015) 3100–3114. doi:10.1016/j.combustflame.2015.02.015.

[8] S.K. Dhanuka, J.E. Temme, J. Driscoll, Unsteady Aspects of Lean Premixed Prevaporized Gas Turbine Combustors: Flame-Flame Interactions, J. Propuls. Power. 27 (2011) 631–641. doi:10.2514/1.B34001.

[9] W. Meier, I. Boxx, M. Stöhr, C.D. Carter, Laser-based investigations in gas turbine model combustors, Exp. Fluids. 49 (2010) 865–882. doi:10.1007/s00348-010-0889-x.

[10] U. Stopper, W. Meier, R. Sadanandan, M. Stöhr, M. Aigner, G. Bulat, Experimental study of industrial gas turbine flames including quantification of pressure influence on flow field, fuel/air premixing and flame shape, Combust. Flame. 160 (2013) 2103–2118.

[11] I. Boxx, C.M. Arndt, C.D. Carter, W. Meier, High-speed laser diagnostics for the study of flame dynamics in a lean premixed gas turbine model combustor, Exp. Fluids. 52 (2012) 555–567. doi:10.1007/s00348-010-1022-x.

[12] M. Stöhr, R. Sadanandan, W. Meier, Phase-resolved characterization of vortex–flame interaction in a turbulent swirl flame, Exp. Fluids. 51 (2011) 1153–1167. doi:10.1007/s00348-011-1134-y.

[13] I. Boxx, C.D. Carter, M. Stöhr, W. Meier, Study of the mechanisms for flame stabilization in gas turbine model combustors using kHz laser diagnostics, Exp. Fluids. 54 (2013). doi:10.1007/s00348-013-1532-4.

[14] M. Stöhr, C.M. Arndt, W. Meier, Transient effects of fuel-air mixing in a partially-premixed turbulent swirl flame, Proc. Combust. Inst. 35 (2015) 3327–3335. doi:10.1016/j.proci.2014.06.095.

[15] C.D. Slabaugh, A.C. Pratt, R.P. Lucht, Simultaneous 5 kHz OH-PLIF/PIV for the study of turbulent combustion at engine conditions, Appl. Phys. B. 118 (2015)

109–130. doi:10.1007/s00340-014-5960-5.
[16] I. Boxx, C. Slabaugh, P. Kutne, R.P. Lucht, W. Meier, 3 kHz PIV/OH-PLIF measurements in a gas turbine combustor at elevated pressure, Proc. Combust. Inst. 35 (2015) 3793–3802. doi:10.1016/j.proci.2014.06.090.
[17] S. Marinov, M. Kern, N. Zarzalis, P. Habisreuther, A. Peschiulli, F. Turrini, O.N. Sara, Similarity issues of kerosene and methane confined flames stabilized by swirl in regard to the weak extinction limit, Flow, Turbul. Combust. 89 (2012) 73–95. doi:10.1007/s10494-012-9392-1.
[18] C.T. Chong, S. Hochgreb, Spray flame structure of rapeseed biodiesel and Jet-A1 fuel, Fuel. 115 (2014) 551–558. doi:10.1016/j.fuel.2013.07.059.
[19] D.E. Cavaliere, J. Kariuki, E. Mastorakos, A comparison of the blow-off behaviour of swirl-stabilized premixed, non-premixed and spray flames, Flow, Turbul. Combust. 91 (2013) 347–372. doi:10.1007/s10494-013-9470-z.
[20] A. Johchi, L. Zimmer, M. Tanahashi, Investigation on the acoustic behavior of a turbulent swirl-stabilized combustor fed with liquid fuel, in: 17th Int. Symp. Appl. Laser Tech. to Fluid Mech., Lisbon, 2014: pp. 7–10.
[21] A. Lantz, R. Collin, J. Sjöholm, Z.S. Li, P. Petersson, M. Aldén, High-speed imaging of fuel/OH distributions in a gas turbine pilot burner at elevated pressure, in: 49th AIAA Aerosp. Sci. Meet. Incl. New Horizons Forum Aerosp. Expo., 2011: p. 13268.
[22] I. Chterev, N. Rock, H. Ek, B. Emerson, J. Seitzman, N. Jiang, S. Roy, T. Lee, J. Gord, T. Lieuwen, Simultaneous imaging of fuel, OH, and three component velocity fields in high pressure, liquid fueled, swirl stabilized flames at 5 kHz, Combust. Flame. 186 (2017) 150–165. doi:10.1016/j.combustflame.2017.07.021.
[23] M. Cordier, A. Vandel, G. Cabot, B. Renou, A.M. Boukhalfa, Laser-induced spark ignition of premixed confined swirled flames, Combust. Sci. Technol. 185 (2013) 379–407. doi:10.1080/00102202.2012.725791.
[24] M. Orain, P. Baranger, C. Ledier, J. Apeloig, F. Grisch, Fluorescence spectroscopy of kerosene vapour at high temperatures and pressures: Potential for gas turbines measurements, Appl. Phys. B Lasers Opt. 116 (2014) 729–745. doi:10.1007/s00340-013-5756-z.
[25] P. Malbois, E. Salaün, B. Rossow, G. Cabot, L. Bouheraoua, S. Richard, B. Renou, F. Grisch, Quantitative measurements of fuel distribution and flame structure in a lean-premixed aero-engine injection system by kerosene/OH-PLIF measurements under high-pressure conditions, Proc. Combust. Inst. (2018). doi:10.1016/j.proci.2018.05.171.
[26] J. Weickert, B.M.T.H. Romeny, M.A. Viergever, Efficient and reliable schemes for nonlinear diffusion filtering, Image Process. IEEE Trans. 7 (1998) 398–410.
[27] H. Malm, G. Sparr, J. Hult, C.F. Kaminski, Nonlinear diffusion filtering of images obtained by planar laser-induced fluorescence spectroscopy, J. Opt. Soc. Am. A-Optics Image Sci. Vis. 17 (2000) 2148–2156. doi:10.1364/JOSAA.17.002148.
[28] R. Abu-Gharbieh, C. Kaminski, T. Gustavsson, G. Hamarneh, Flame front matching and tracking in PLIF images using geodesic\npaths and level sets, in: Proc. IEEE Work. Var. Lev. Set Methods Comput. Vis., 2001: pp. 112–118. doi:10.1109/VLSM.2001.938889.
[29] P. Perona, J. Malik, Scale-space and edge detection using anisotropic diffusion,

IEEE Trans. Pattern Anal. Mach. Intell. 12 (1990) 629–639. doi:10.1109/34.56205.
[30] N. Otsu, A threshold selection method from gray-level histograms, IEEE Trans. Syst. Man. Cybern. 9 (1979) 62–66. doi:10.1109/TSMC.1979.4310076.
[31] L. Sirovich, Turbulence and the dynamics of coherent structures, Q. Appl. Math. 45 (1987) 561–571. doi:10.3109/10717544.2013.779332.
[32] R.J. Adrian, K.T. Christensen, Z.-C. Liu, Analysis and interpretation of instantaneous turbulent velocity fields, Exp. Fluids. 29 (2000) 275–290.
[33] J. Samarasinghe, S.J. Peluso, B.D. Quay, D. a Santavicca, The three-dimensional structure of swirl-stabilized flames in a lean premixed multinozzle can combustor, in: Proc. ASME Turbo Expo 2015 Turbine Tech. Conf. Expo. GT2015-42167, 2015: pp. 1–12.
[34] I. Papamoschou, A. Roshko, The compressible turbulent shear layer : an experimental study, J . Fluid Mech. 197 (1987) 453–477. doi:10.1017/S0022112088003325.
[35] P.E. Dimotakis, G.L. Brown, The mixing layer at high Reynolds number: large-structure dynamics and entrainment, J. Fluid Mech. 78 (1976) 535–560. doi:10.1017/S0022112076002590.
[36] Q. An, W.Y. Kwong, B.D. Geraedts, A.M. Steinberg, Coupled dynamics of lift-off and precessing vortex core formation in swirl flames, Combust. Flame. 168 (2016) 228–239. doi:10.1016/j.combustflame.2016.03.011.
[37] J.P. Moeck, J.F. Bourgouin, D. Durox, T. Schuller, S. Candel, Nonlinear interaction between a precessing vortex core and acoustic oscillations in a turbulent swirling flame, Combust. Flame. 159 (2012) 2650–2668. doi:10.1016/j.combustflame.2012.04.002.
[38] R. Sadanandan, M. Stöhr, W. Meier, Simultaneous OH-PLIF and PIV measurements in a gas turbine model combustor, Appl. Phys. B Lasers Opt. 90 (2008) 609–618. doi:10.1007/s00340-007-2928-8.
[39] R. Mercier, T.F. Guiberti, A. Chatelier, D. Durox, O. Gicquel, N. Darabiha, T. Schuller, B. Fiorina, Experimental and numerical investigation of the influence of thermal boundary conditions on premixed swirling flame stabilization, Combust. Flame. 171 (2016) 42–58. doi:10.1016/j.combustflame.2016.05.006.
[40] P. Malbois, E. Salaün, F. Frindt, G. Cabot, B. Renou, F. Grisch, Experimental investigation with optical diagnostics of a LP aero-engine injection system under relevant operating conditions, in: Proc. ASME Turbo Expo 2017 Turbiomachinery Tech. Conf. Expo. GT2017-64484, Chatlotte (N.C), 2017: pp. 1–14.
[41] J.M. Donbar, J.F. Driscoll, C.D. Carter, Reaction zone structure in turbulent nonpremixed jet flames - From CH-OH PLIF images, Combust. Flame. 122 (2000) 1–19. doi:10.1016/S0010-2180(00)00098-5.
[42] G. Joulin, G.I. Sivashinsky, Pockets in premixed flames and combustion rate, Combust. Sci. Technol. 77 (1991) 329–335. doi:10.1080/00102209108951735.
[43] M. Tanahashi, S. Taka, M. Shimura, T. Miyauchi, CH double-pulsed PLIF measurement in turbulent premixed flame, Exp. Fluids. 45 (2008) 323–332. doi:10.1007/s00348-008-0482-8.
[44] S. Dhanuka, J. Driscoll, H. Mongia, Instantaneous flow structures in a reacting gas turbine combustor, in: 44th AIAA/ASME/SAE/ASEE Jt. Propuls. Conf.

Exhib., Hartford, 2008. doi:doi:10.2514/6.2008-4683.
[45] T. Ueda, M. Shimura, M. Tanahashi, T. Miyauchi, Measurement of three-dimensional flame structure by combined laser diagnostics, J. Mech. Sci. Technol. 23 (2009) 1813–1820. doi:10.1007/s12206-009-0608-9.
[46] R. Borghi, S.N.B. Murthy, Turbulent reactive flow, Springer-Verlag, 1989.
[47] Y. Nada, M. Tanahashi, T. Miyauchi, Effect of turbulence Characteristics on lacal structure of H2-air premixed flames, J. Turbul. 5 (2003).
[48] N. Peters, Laminar flamelet concepts in turbulent combustion, in: Symp. Combust., Combustion Institute, 1986: pp. 1231–1250. doi:10.1016/S0082-0784(88)80355-2.
[49] T. Poinsot, D. Veynante, S. Candel, Quenching process and premixed turbulent combustion diagrams, J. Fluid Mech. 228 (1991) 561–606.
[50] B. Franzelli, A. Vié, M. Ihme, Characterizing the regimes of spray flame-vortex interactions : a spray spectral diagram for extinction and re-ignition, ILASS Eur. 26th Annu. Conf. Liq. At. Spray Syst. (2014) 8–10.

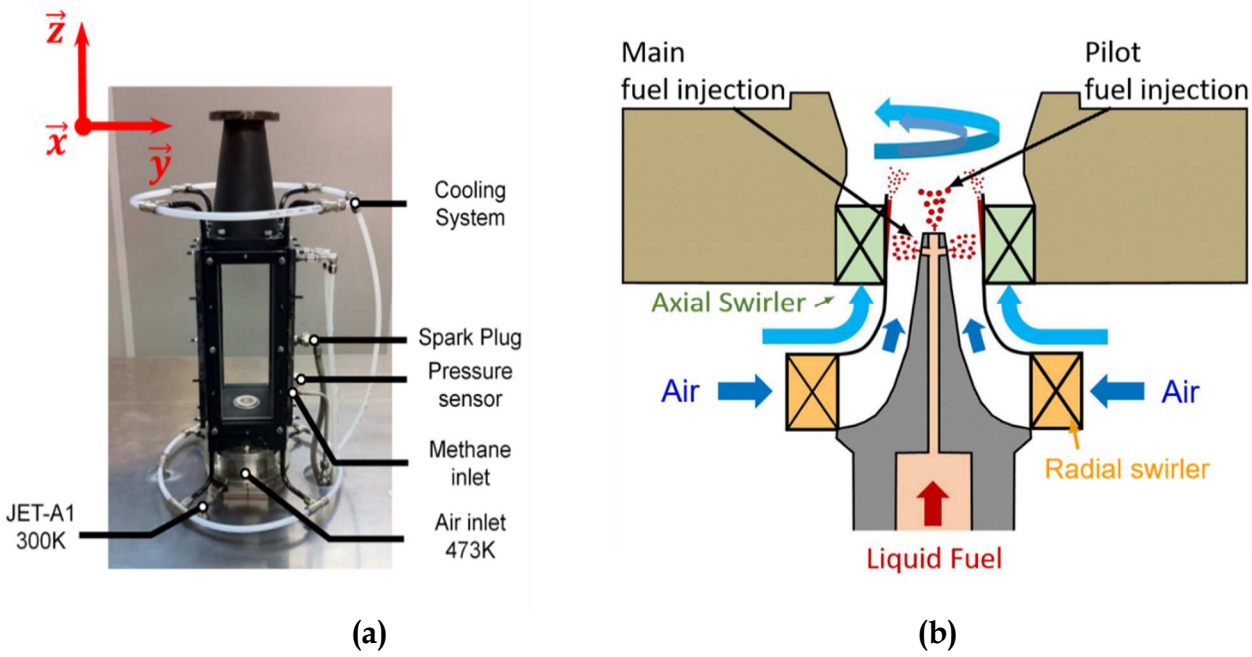

(a) **(b)**

Fig. 1. (a) Combustion facility equipped with the LP injection system. **(b)** General schematic of the LP injection system

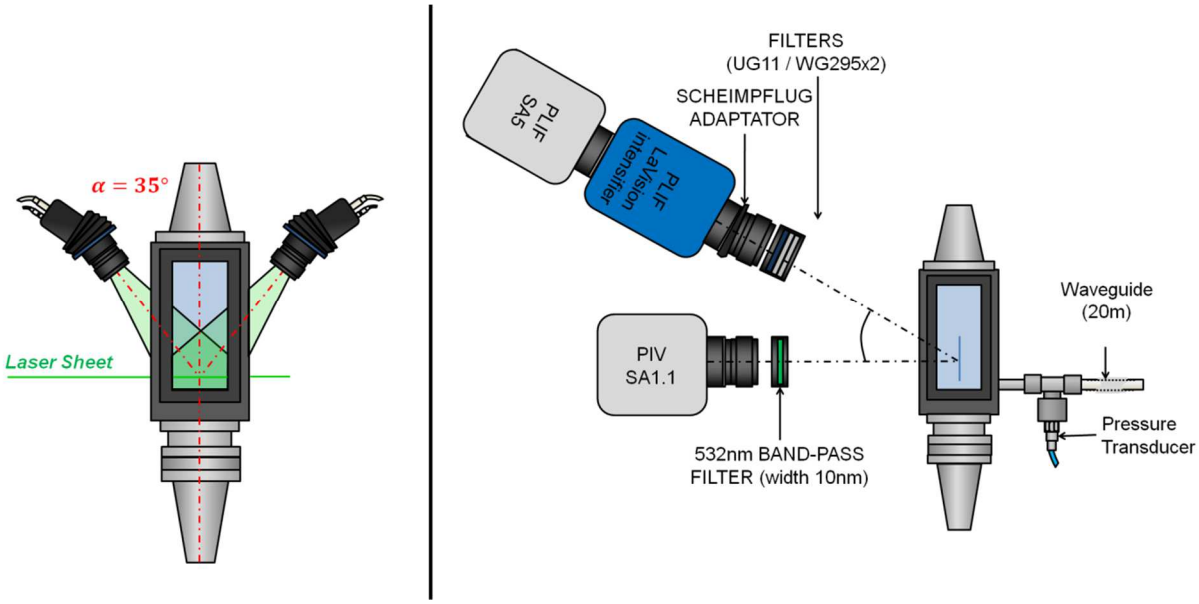

Fig. 2. Experimental set-up for **(a)** radial stereo-PIV, **(b)** joint high-speed OH-PLIF and PIV

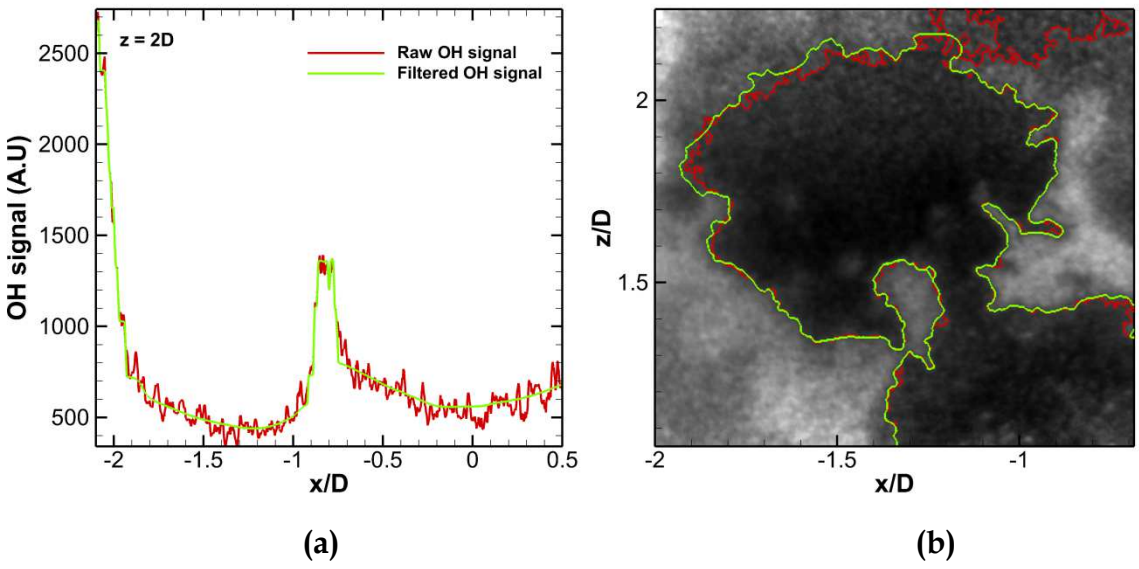

Fig. 3. (a) Intensity profile before (red) and after (green) filtering at z/D = 2, **(b)** Contour detection using Otsu's method before and after filtering the OH image.

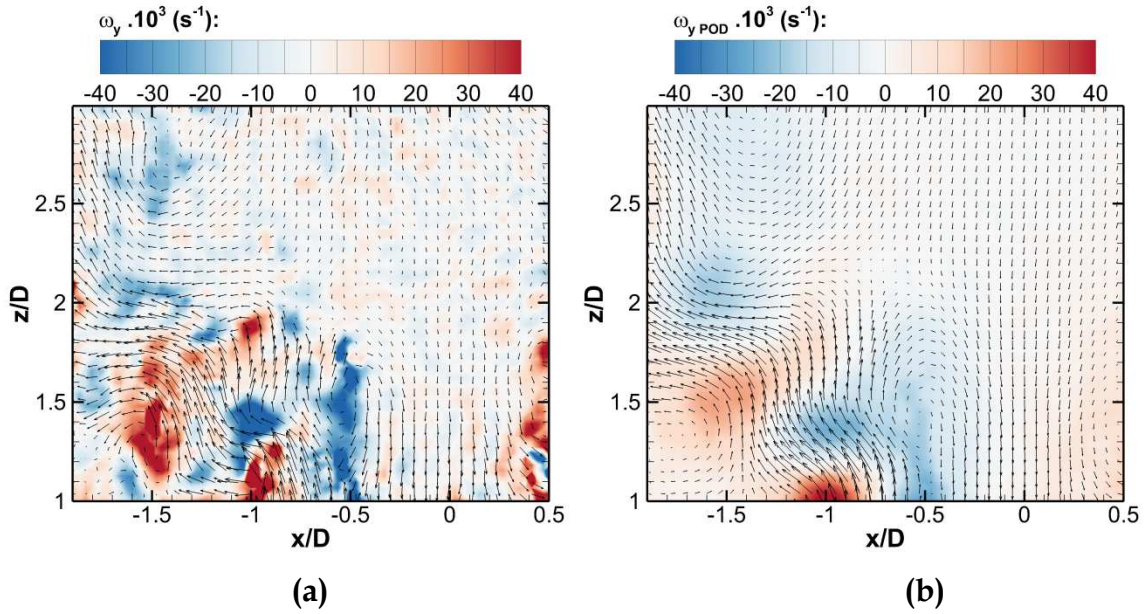

Fig. 4. (**a**) Instantaneous vorticity field, **(b)** 50 modes POD reconstruction and energy mode diagram. (1 arrow out of 2 is plotted).

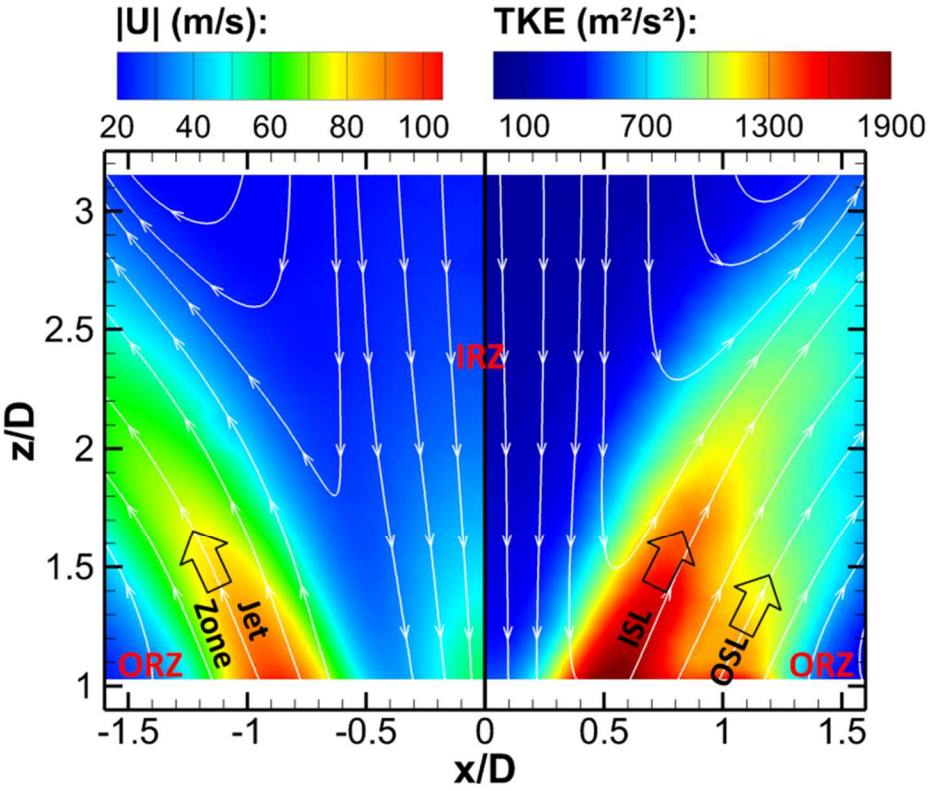

Fig. 5. Streamlines of the averaged 2D flow velocity colored by: **(a)** norm of the averaged velocity field and **(b)** turbulent kinetic energy.

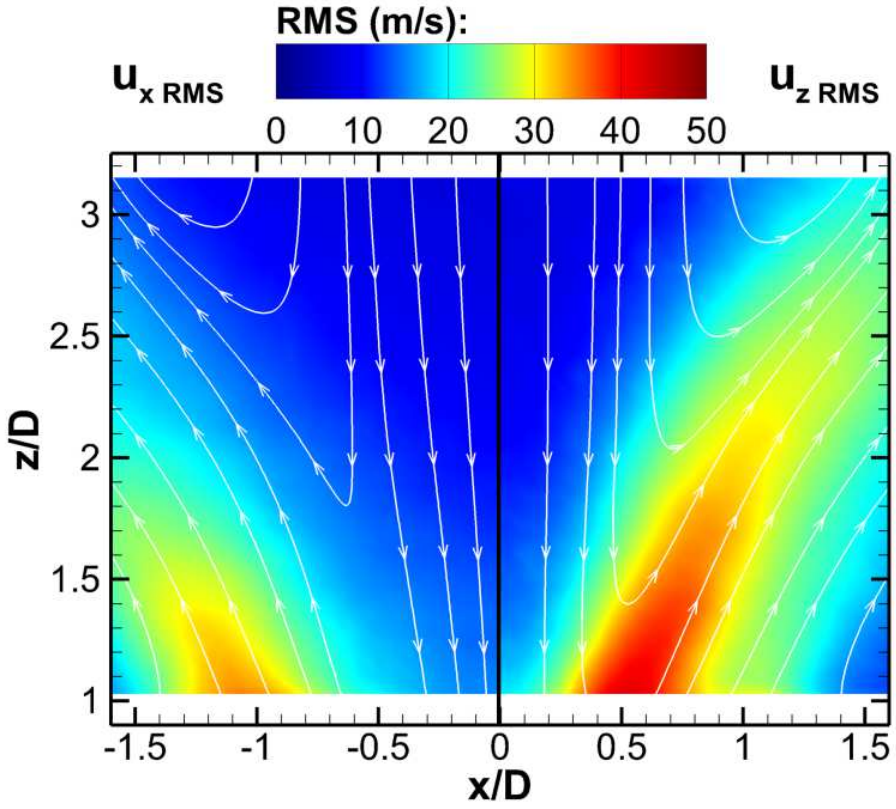

Fig. 6. Streamlines of the averaged 2D flow velocity colored by: **(a)** RMS of the radial velocity u_x **(b)** RMS of the axial velocity u_z.

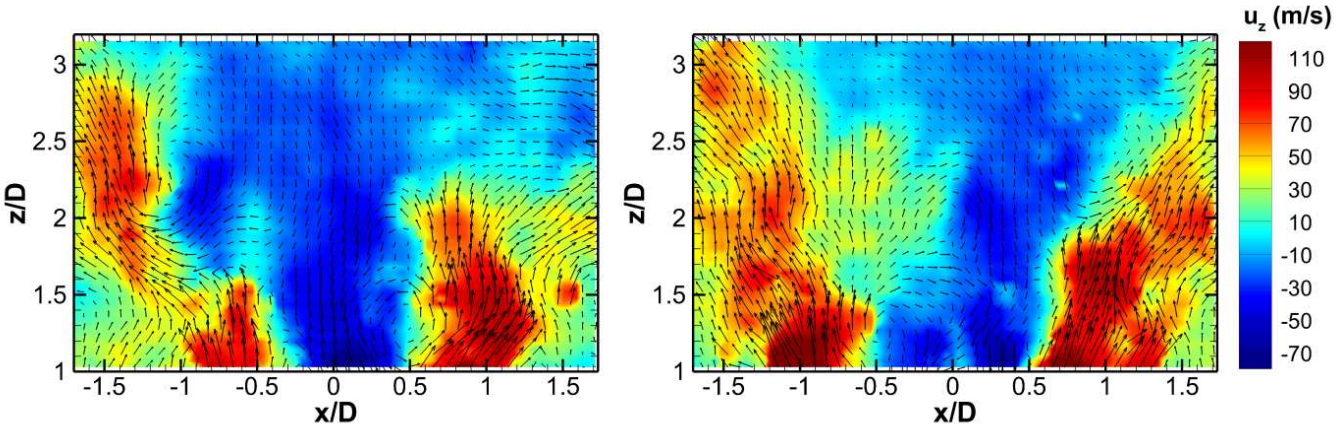

Fig. 7. Typical instantaneous flow fields colored by the axial velocity u_z.

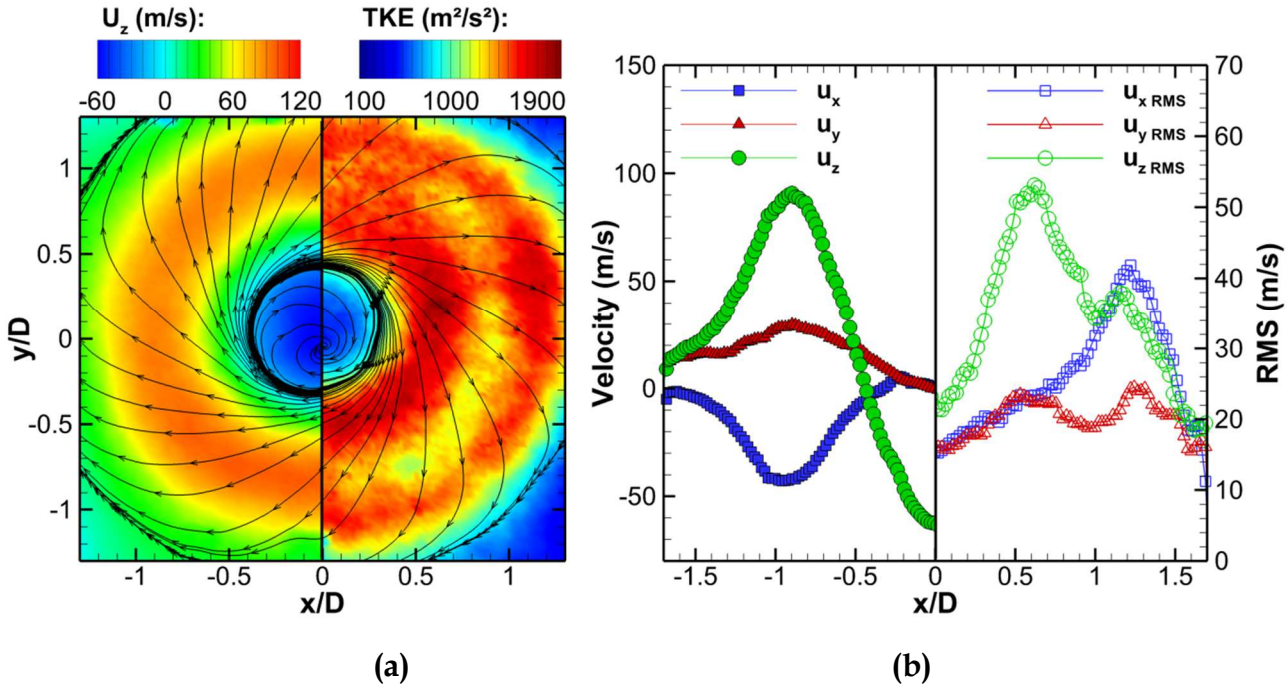

Fig. 8: (a) Streamlines of the averaged 2D flow velocity distribution at z/D= 1.1 colored by (left) the average of the axial flow velocity and (right) TKE. **(b)** Averaged and rms radial flow velocity profiles at y/D= 0, z/D = 1.1**.**

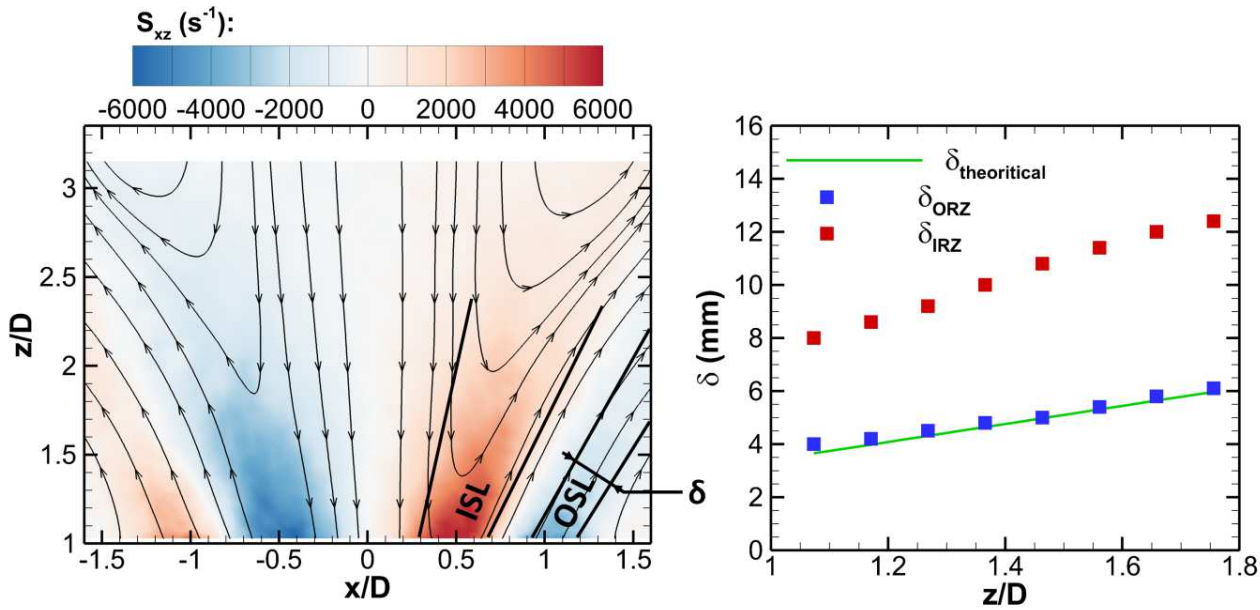

(a) **(b)**

Fig. 9. (a) Mean in plane strain rate S_{xz} , **(b)** Comparison of the theoretical shear layer thickness driven by Kelvin-Helmholtz instabilities (green line) with the experimental shear layer thickness in the ORZ (blue squares) and in the IRZ (red diamonds).

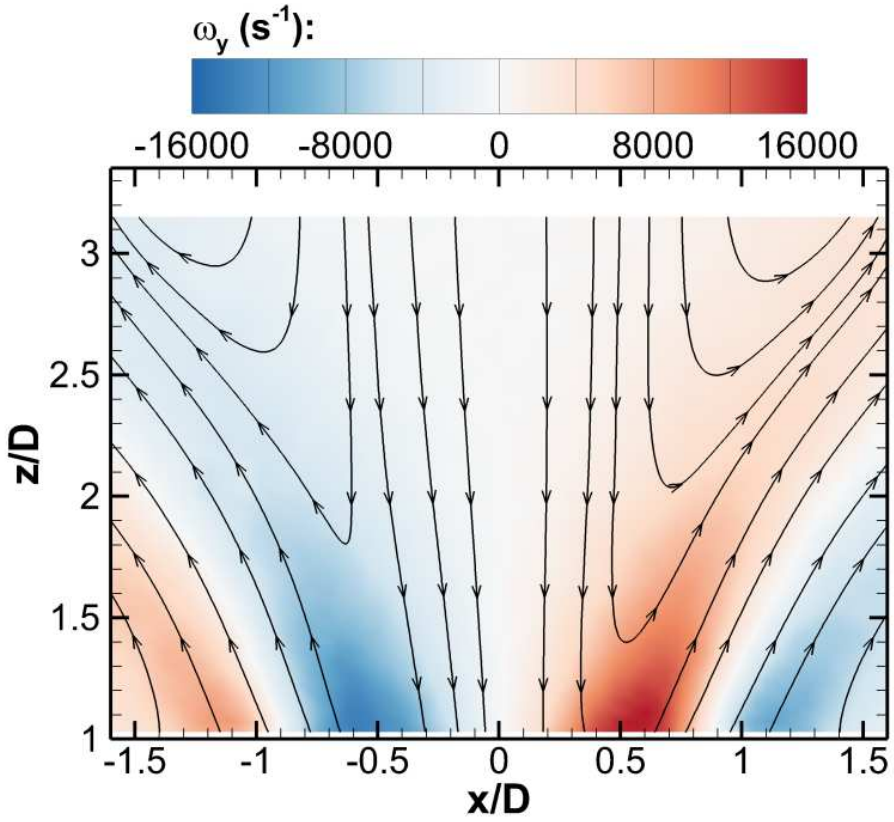

Fig. 10. Mean Out of plane vorticity $\overline{\omega_y}$

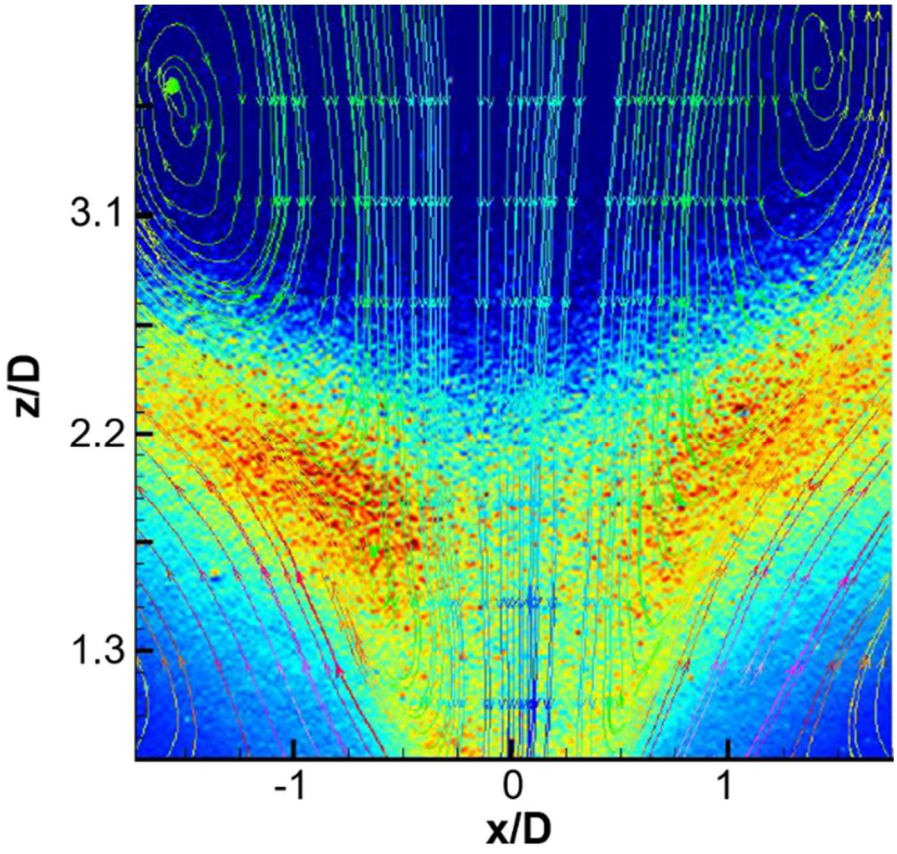

Fig. 11. Time averaged OH* chemiluminescence image after Abel transform

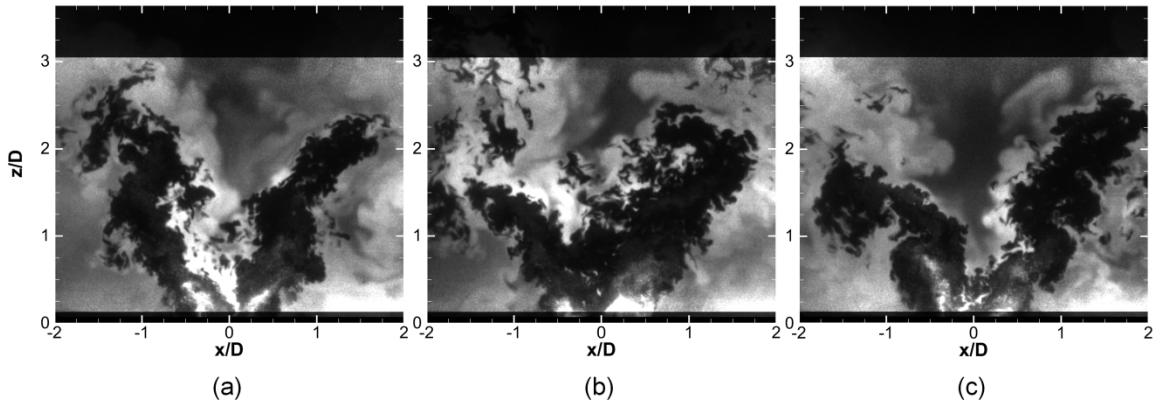

Fig. 12. Typical instantaneous OH-PLIF images corrected from the laser energy distribution.

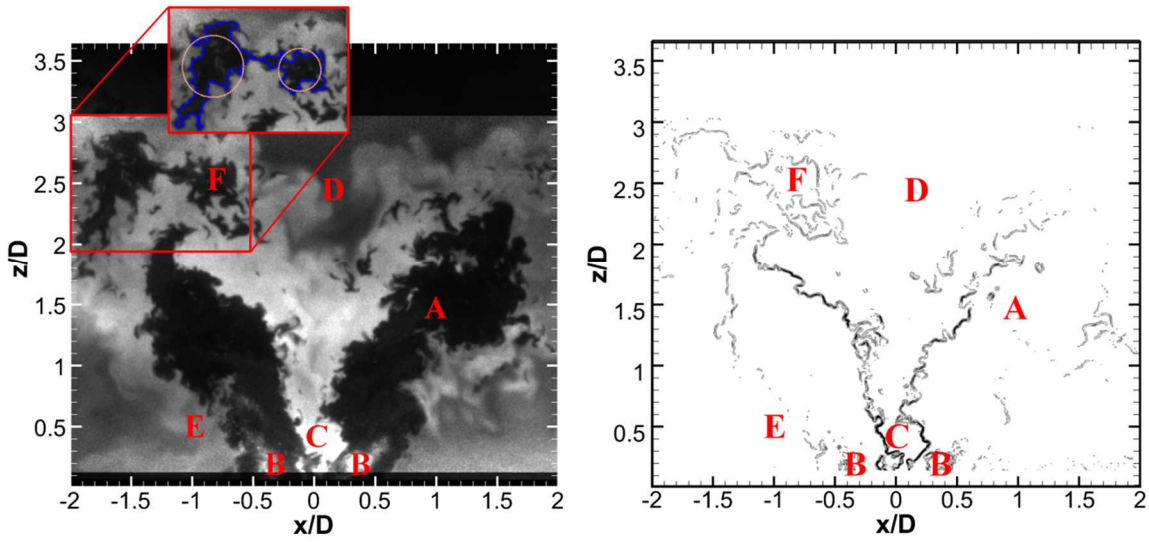

Fig. 13. (a) Instantaneous corrected OH-PLIF image, **(b)** associated OH-gradient image.

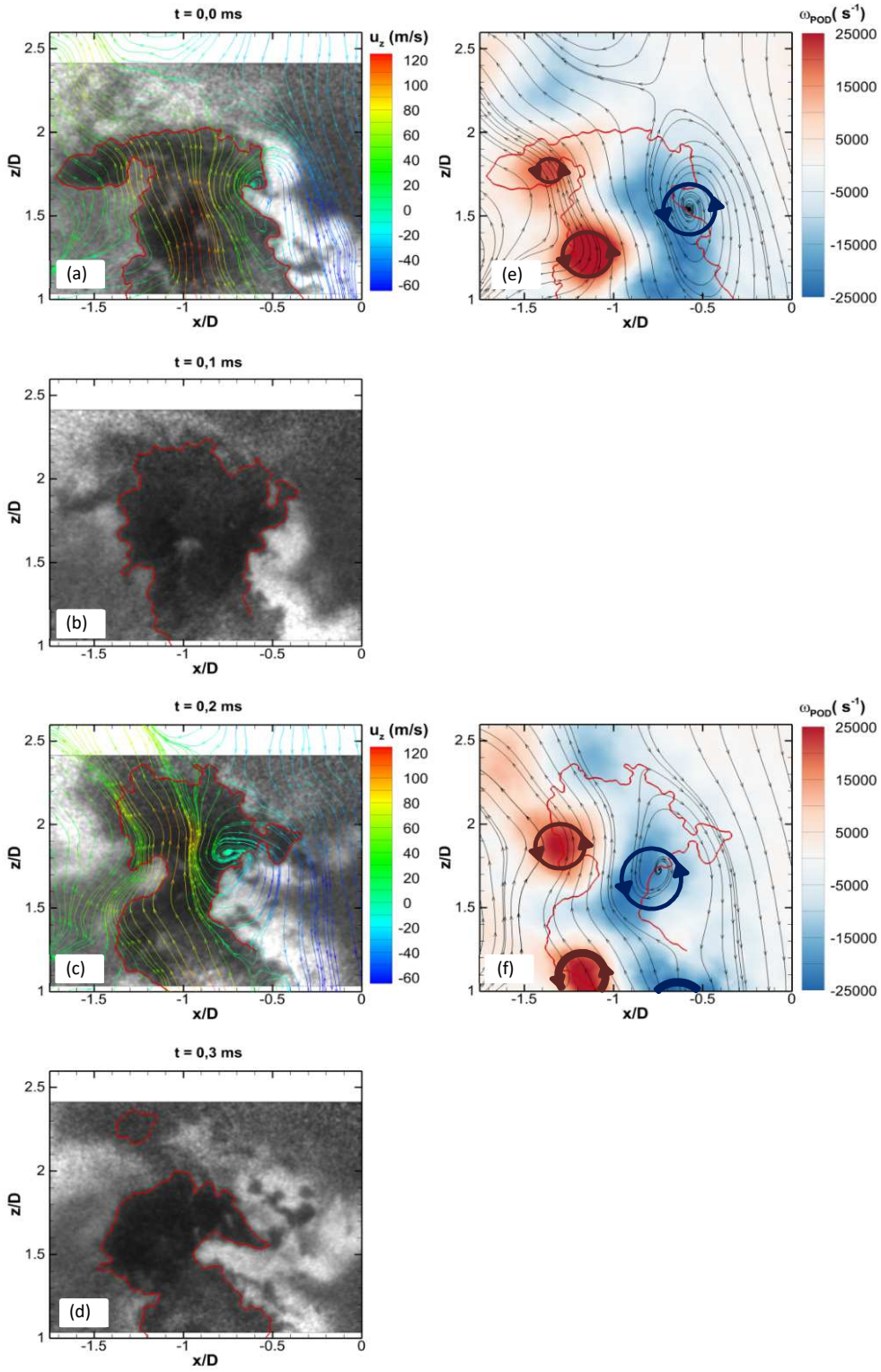

Fig. 14. Time sequence of flame splitting event **(Left row)** OH-PLIF time-series images superimposed with the velocity field coloured by the axial flow velocity. **(Right row)** Streamlines of POD reconstructed velocity fields coloured by vorticity. Red lines represent the contour of the flame. The schematic positions of vortices are indicated on the vorticity images.

	Acquisition Rate (Hz)	Resolution (pixels)	Magnification ratio (mm/pixel)	ROI (L x H) (mm x mm)
S-PIV	5	2048 x 2048	0.0364	60 x 70
OH-PLIF	3.33	1024 x 1024	0.0830	76 x 60
kHz OH-PLIF	10 000	896 x 848	0.0857	76 x 30
kHz PIV	5 000	768 x 768	0.1100	76 x 50

Table 1: Experimental parameters.

6 Supplementary Materials

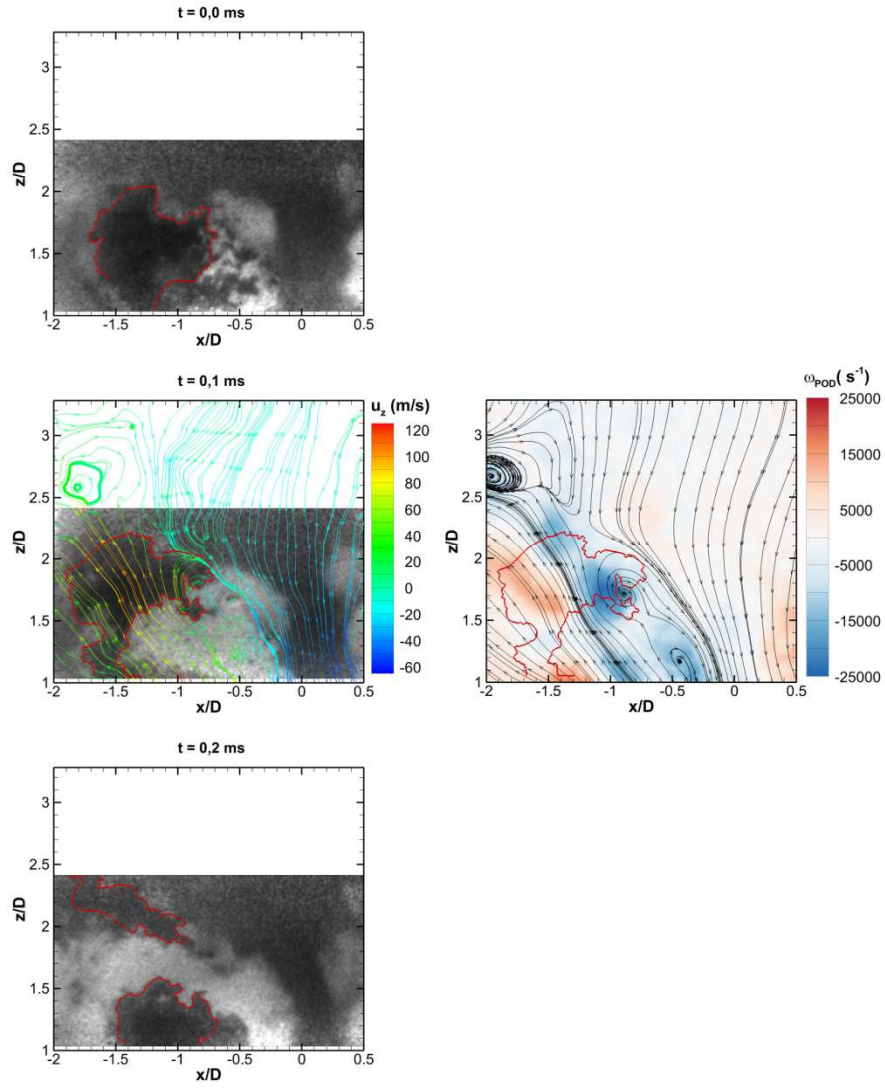

Time sequence of flame splitting event (Left row) OH-PLIF time-series images superimposed with the velocity field coloured by the axial flow velocity. (Right row) Streamlines of POD reconstructed velocity fields coloured by vorticity. Red lines represent the contour of the flame.

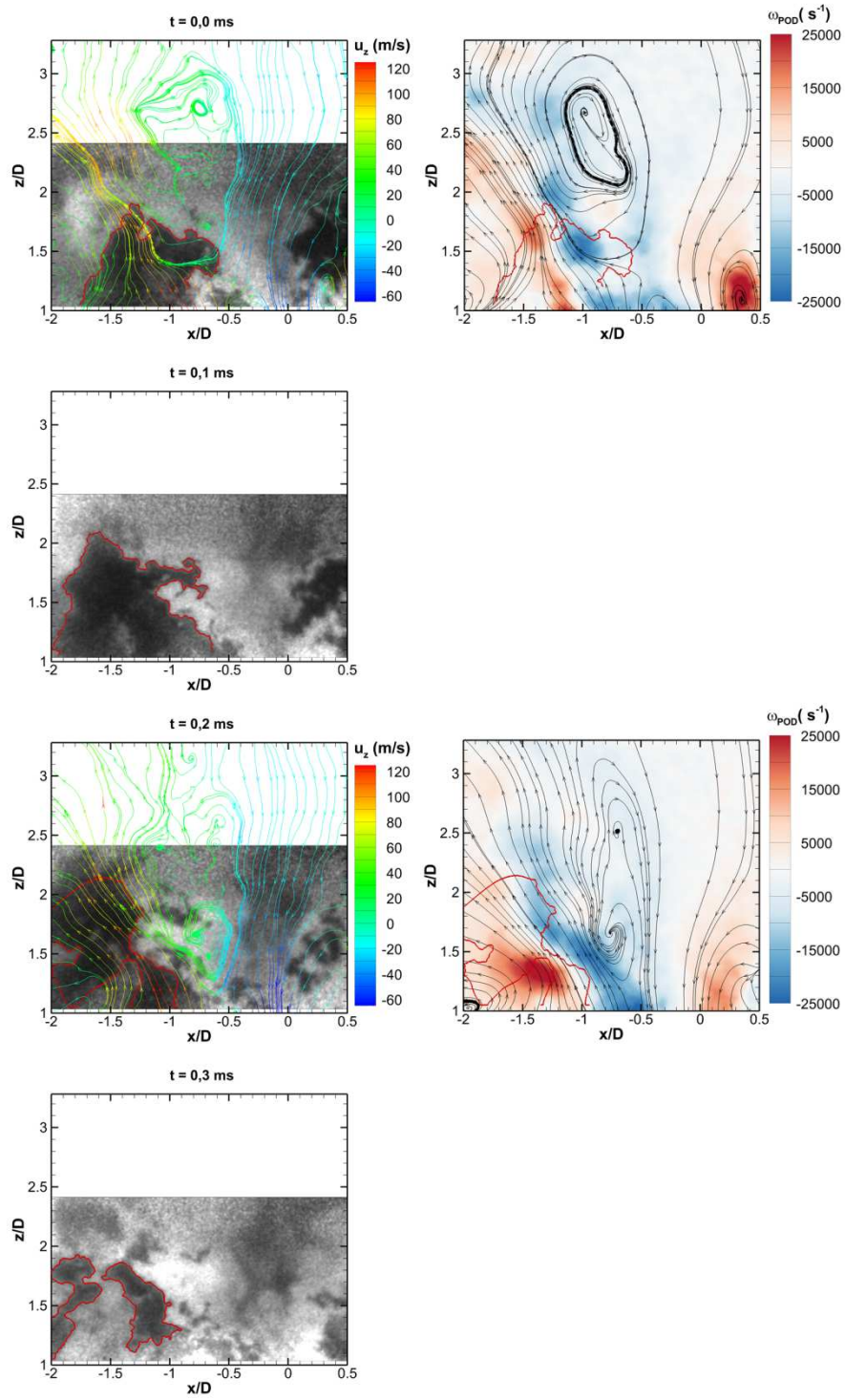

Time sequence of flame splitting event (Left row) OH-PLIF time-series images superimposed with the velocity field coloured by the axial flow velocity. (Right row) Streamlines of POD reconstructed velocity fields coloured by vorticity. Red lines represent the contour of the flame.